Inorganic Chemistry

Article

pubs.acs.org/IC

Proton-Induced Disproportionation of a Ruthenium Noninnocent Ligand Complex Yielding a Strong Oxidant and a Strong Reductant

Maria Kapovsky, Christopher Dares, Elaine S. Dodsworth, Rowshan Ara Begum, Vanessa Raco, and A. B. P. Lever*

Department of Chemistry, York University, 4700 Keele St., Toronto, Ontario, Canada M3J1P3

S *Supporting Information*

ABSTRACT: The complex $Ru^{II}(NH_3)_2(o\text{-benzoquinonediimine})Cl_2$ undergoes a reversible apparent acid/base reaction, although it has no obvious basic lone pairs. The reaction is a proton-assisted disproportionation yielding an oxidant ($[Ru^{III}(NH_3)_2(o\text{-benzoquinonediimine})Cl_2]^+$) and a reductant ($[Ru^{III}(NH_3)_2(o\text{-phenylenediamine})Cl_2]^+$). These species were characterized by electrochemistry, ultraviolet–visible light (UV-vis), vibrational (infrared (IR) and Raman), mass and electron paramagnetic resonance (EPR) spectroscopy, and X-ray structural analysis. The reaction is shown to be downhill from an isodesmic calculation. Three different isosbestic interconversions of the parent and product species are demonstrated. The electronic structures of these species were analyzed, and their optical spectra assigned, using density functional theory (DFT) and time-dependent DFT. This disproportionation of a noninnocent ligand complex may be relevant to the application of noninnocent ligands in organometallic catalysis and in the biological milieu.

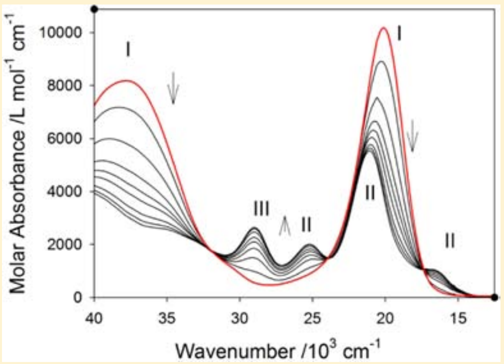

INTRODUCTION

Noninnocent ligands have been recognized, in recent years, to play prominent roles in biological systems.[1−22] The very unusual disproportionation reported here simultaneously generates stable oxidizing and reducing agents, related by a two-electron process. This may be considered to be a proton-induced charge separation that produces reactive but stable species. We previously reported[23] the synthesis and properties of the species $Ru^{II}(NH_3)_2(bqdi)Cl_2$ (**I**) (bqdi = *o*-benzoquinonediimine). This highly covalent molecule, which has no free protonatable sites, reacts with dilute mineral acids in a reversible manner. Thus, the very simple ultraviolet–visible light (UV-vis) spectrum changes to a much richer spectrum (Figure 1) upon the addition of acid but reverts to the same original simple spectrum when the solution is neutralized. Essentially the same behavior is seen with hydrochloric, nitric, sulfuric, and phosphoric acids, in water or in water-miscible organic solvents, etc. Thus, the counterion is irrelevant. The system is also stable in cold concentrated hydrochloric or sulfuric acid, yielding essentially the same complex UV-vis spectrum.

We demonstrate below that this is not a simple acid–base reaction but is, in fact, a *proton-induced disproportionation* whereby the metal is oxidized and one ligand is reduced.

The reaction may be written as

$$\underset{2(\mathbf{I})}{2Ru^{II}(NH_3)_2(bqdi)Cl_2} + 2H^+ \rightarrow \underset{(\mathbf{II})}{[Ru^{III}(NH_3)_2(bqdi)Cl_2]^+} + \underset{(\mathbf{III})}{[Ru^{III}(NH_3)_2(opda)Cl_2]^+} \quad (1)$$

where opda =1,2-phenylenediamine.

There are isosbestic points in the spectroscopic conversion (Figure 1). Such an observation is commonly believed to indicate that only two species are present in solution; however, as discussed previously by Drago,[24] there are conditions where three or more species in equilibrium may generate isosbestic points. This is an example where three species are involved (but see below). In Figure 1, absorption labeled "I" belongs to the parent species (**I**), that labeled "II" is assigned to species **II**, and that labeled "III" is associated with species **III**.

Species **II** is derived from **I** by one electron oxidation, while species **III** involves two-electron reduction of bqdi and subsequent protonation to form ligated 1,2-phenylenediamine (opda), accompanied by oxidation of Ru^{II} to Ru^{III}, i.e., net one electron reduction with the addition of two protons.

The reaction proceeds rapidly in very strong acid, but relatively slowly in dilute acid. Thus, in 0.001 M HCl, there is time, using a diode array spectrometer, to collect a series of optical spectra as the species convert.

It proved possible to define synthetic conditions that allow for the separate recovery of the two species. We report

Received: July 19, 2012
Published: December 17, 2012

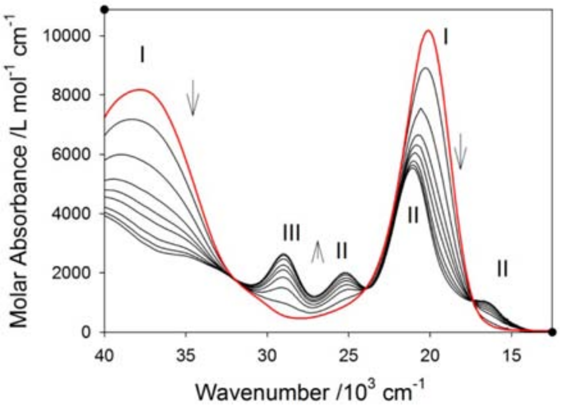

Figure 1. Reaction of $[Ru^{II}(NH_3)_2(bqdi)Cl_2$ (**I**) (red) in methanol with a few drops of concentrated HCl to form $[Ru^{III}(NH_3)_2(bqdi)Cl_2]^+$ (**II**) and $[Ru^{III}(NH_3)_2(opda)Cl_2]^+$ (**III**). See text for annotation. Isosbestic points occur at 17 360, 23 930, and 32 040 cm^{-1}.

electronic and vibrational data (IR), mass spectra, cyclic voltammetry, electron paramagnetic resonance (EPR), X-ray structural characterization, and density functional theory (DFT) analysis of the new species **II** and **III** and magnetism and resonance Raman data for species **II**.

■ RESULTS AND DISCUSSION

Syntheses of $[Ru^{III}(NH_3)_2(bqdi)Cl_2]Cl$ (II) and $[Ru^{III}(NH_3)_2(opda)Cl_2]Cl$ (III). Species **II** is obtained from the parent species (**I**) by treatment with concentrated hydrochloric acid, in which it is almost insoluble. The resulting black/deep green solid (**II**) is analytically pure. Its identity as a simple Ru^{II}-to-Ru^{III} oxidation product of species **I** is assured from CHN analysis, mass spectrum (see the Experimental Section), magnetic data (low-spin d^5), and the crystal structure described below. It may also be obtained by spectroelectrochemical oxidation (Figure 2) or chemical oxidation of species **I** with $AgNO_3$ (see the Supporting Information).

$[Ru^{III}(NH_3)_2(bqdi)Cl_2]^+$ (**II**) is soluble in methanol, yielding a green solution that is fairly stable. It is sparingly soluble in acetonitrile and in water, enough to monitor its spectrum in a cuvette, but reconverts to species **I** over a period of days, or rapidly if base is added. In water containing 1 M (or stronger) HCl, it is indefinitely stable. The infrared spectrum shows two sharp peaks at 3257 and 3340 cm^{-1}, which are due to the symmetric and antisymmetric N−H (bqdi) stretching vibrations, compared to the peaks observed at 3234 and 3327 cm^{-1} for the Ru^{II} species (**I**).

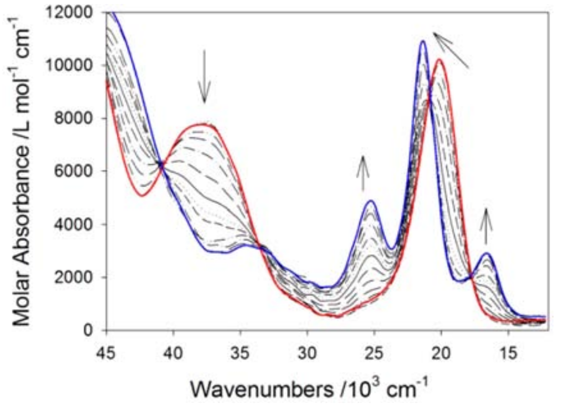

Figure 2. Spectroelectrochemical oxidation of $Ru^{II}(NH_3)_2(bqdi)Cl_2$ (**I**) (red) in methanol/$TBAPF_6$ at +0.8 V vs SCE to yield $[Ru^{III}(NH_3)_2(bqdi)Cl_2]^+$ (**II**) (blue). Isosbestic points occur at 17 790, 20 860, 33 500, and 40 900 cm^{-1}.

The pink cationic $[Ru^{III}(NH_3)_2(opda)Cl_2]^+$ species (**III**) is retrieved from the filtrate of the concentrated HCl reaction with **I** noted above. Freeze-drying of the initial filtrate from HCl yielded the chloride salt. However, this species is very unstable. It reconverts to species **I** in pure water on a time scale of minutes, and instantaneously if base is added. Attempts to wash the sample in preparation for CHN analysis always caused some contamination with species **I** or **II**, as confirmed by the electronic spectra. Its identity is ensured by its mass spectrum (see the Experimental Section) and the crystal structure of the zincate salt. It shows broad structured absorption in the NH stretching region of the IR spectrum.

X-ray Structures. The $[Ru^{III}(NH_3)_2(bqdi)Cl_2][Cl]$ (**II**) complex (see Table 1 and Figure 3, left) crystallizes in a very similar manner to $[Ru^{II}(NH_3)_2(bqdi)Cl_2]$ (**I**).[23] Both crystallize in the *Pnma* space group with the ruthenium complex lying on plane *m*. The $Ru-N_{NH_3}$ bond length is 2.135 Å, which is nearly unchanged from the Ru^{II} species, while the Ru−Cl bond lengths are contracted by ca. 0.05 Å, to an average of 2.33 Å. The $Ru-N_{bqdi}$ distance is 1.985 Å, which is 0.02 Å longer than in the reduced species. The C−C distances alternate between short and long, as expected for the bqdi ligand, and are essentially unchanged from the Ru^{II} crystal. The Cl−Ru—Cl angle is 175°, with the Cl atoms pushed slightly away from the bqdi ligand. The bqdi ligand is essentially planar; however, there is an angle of 11° between the plane of the benzoquinone ring and the $Ru-N_{bqdi}$ plane. It is likely that this bend is due to packing effects.

The $[Ru^{III}(NH_3)_2(opda)Cl_2]$ $[ZnCl_3(H_2O)]$ (**IIIc**) complex (see Table 1 and Figure 3, right) crystallizes in the $P2_1/c$ space group, with one unique cation and anion within the unit cell. The average $Ru-N_{opda}$ distance is 2.091 Å, which is much greater than that in the bqdi analogue (**II**) of 1.985 Å. The $Ru-N_{NH_3}$ distances have contracted slightly, with respect to **II**, to 2.113 Å. The Ru−Cl bond lengths remain nearly the same at 2.34 Å, while the Cl−Ru−Cl angle is nearly linear at 175.2°. The C−N distance has increased to 1.462 Å, which is indicative of an aromatic C−N bond. The C−C bonds are all approximately 1.38 Å, indicating that we do not have a quinonoid structure but a delocalized phenyl ring, which is indicative of opda. The opda is planar, but is canted out of the N_4 plane, such that the interplanar angle is 18.2°. The aquatrichlorozincate(II) anion[25−27] has Zn−Cl distances of 2.24 Å, and a $Zn-O_{H_2O}$ distance of 2.01 Å. Selected bond distances for $[Ru^{II}(NH_3)_2(bqdi)Cl_2]$ (**I**), and species **II** and **IIIc**, are shown in Table 2.

Cyclic voltammetry. The cyclic voltammograms of species **II** and **III** in methanol are shown in Figure 4.

The data were internally corrected using the Fc^+/Fc couple, which is assumed to lie at 0.346 V vs SCE (0.102 V vs NHE) in methanol (MeOH).[28] The small wave near 0.5 V in the voltammogram of **III** is due to the slight decomposition to species **I**. The current scale is arbitrary.

One expects that the cyclic voltammogram of species **II** will look identical to that of the parent species (**I**),[23] aside from displacement on the current axis, and that is the case. Wave A (0.49 V vs NHE) is then simply the Ru$^{III/II}$ process with the

Table 1. Summary of Crystal Data and Refinement Results for $[Ru(NH_3)_2(bqdi)Cl_2][Cl]$ (**II**) and $[Ru(NH_3)_2(opda)Cl_2][Zn(OH_2)Cl_3]$ (**IIIc**)

	II	IIIc
empirical formula	$(C_6H_{12}Cl_2N_4Ru)(Cl)$	$(C_6H_{14}Cl_2N_4Ru)$ (H_2OCl_3Zn)
formula weight, fw	347.62	503.92
temperature (K)	150(1)	150(1)
wavelength (Å)	0.71073	0.71073
cryst dimensions (mm)	0.20 × 0.10 × 0.06	0.30 × 0.20 × 0.07
crystal shape, color	needle, brown	needle, purple
crystal system	orthorhombic	monoclinic
space group	*Pnma*	$P2_1/c$
unit-cell dimensions		
a (Å)	8.1451(3)	6.7263(3)
b (Å)	8.8999(5)	13.0769(3)
c (Å)	16.0424(10)	18.2430(8)
α (deg)	90	90
β (deg)	90	94.267(2)
γ (deg)	90	90
volume ($Å^3$)	1162.92(11)	1600.19(11)
Z	4	4
calcd density ($g\ cm^{-3}$)	1.985	2.092
abs coeff (mm^{-1})	2.005	3.27
F(000)	684	988
θ range (deg)	2.6−27.5	2.6−27.5
limiting indices	$-10 < h < 10$	$-8 < h < 8$
	$-11 < k < 11$	$-14 < k < 16$
	$-19 < l < 20$	$-17 < l < 23$
reflns collected/unique/$I > 2\sigma(I)$	10090/1427/925	10488/3637/2903
completeness to θ (%)	99.9	98.9
max. and min transmission	0.903, 0.676	0.803, 0.440
data/params/restraints	1427/71/0	3637/173/0
GOF on F^2	1.12	1.04
R indices ($[F^2 > 2\sigma(F^2)]$)	*R*1 = 0.0530	*R*1 = 0.0407
weighted *R* indices ($[F^2 > 2\sigma(F^2)]$)	*wR*2 = 0.139	*wR*2 = 0.0944
R indices (all data)	*R*1 = 0.1021	*R*1 = 0.0565
Largest residual diff. peak and hole ($e\ Å^3$)	1.70, −1.18	1.44, −1.26

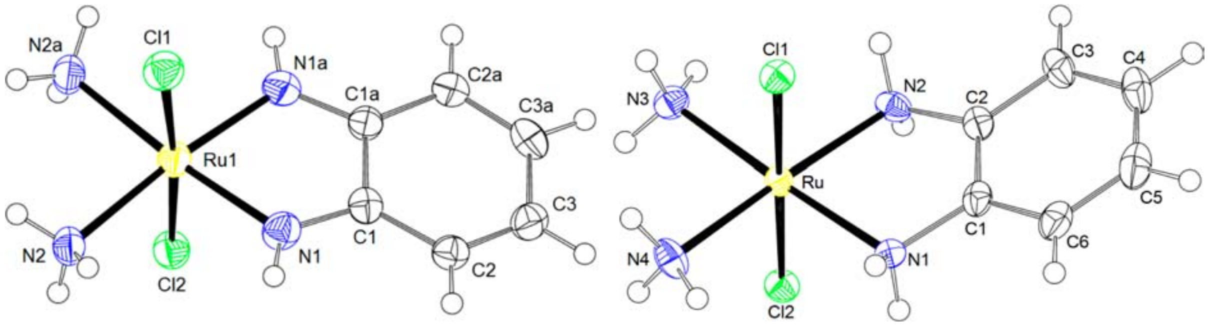

Figure 3. ORTEP rendering of **II** (left) and **IIIc** (right) with thermal displacement ellipsoids drawn at the 50% probability level.

$[Ru(NH_3)_2Cl_2]$ fragment attached to *o*-benzoquinonediimine. No other processes are observed or expected in the range studied.

The characteristic feature of species **III** is wave B (−0.20 V vs NHE) located ca. 0.7 V negative of wave A. The ligand electrochemical parameter[29] (E_L(L)) can be used to predict the expected $Ru^{III/II}$ potential, for any ruthenium (or other metal) complex, using the known E_L(L) values for the ligands. E_L(bqdi), is 0.41 V[23] for species **I** and **II**. The E_L(opda) value has not been reported; however, as a primary amine, it will most likely have a value in the range of 0.06 ± 0.05 V (vs NHE).[29] Assuming the observed wave at −0.20 V vs NHE is the $Ru^{III/II}$ potential for species **III**, we then derive E_L(opda) = 0.07 V vs NHE, well within the expected range. Thus, wave B is so assigned. There are no obvious oxidation waves more positive than 0.3 V vs Fc^+/Fc within the range studied.

Magnetochemistry of $[Ru^{III}(NH_3)_2(bqdi)Cl_2][Cl]$ (II). At room temperature, the χT value of 0.45 $cm^3\ K\ mol^{-1}$ (1.90 μ_B) $4d^5$ recorded for species **II** is slightly higher than the expected theoretical value of 0.375 $cm^3\ K\ mol^{-1}$ for one low-spin Ru^{III} ion, assuming $g = 2$ (see Figure S4 (left) in the Supporting Information). This indicates a slightly larger *g*-value for **II**, consistent with the EPR data (vide infra). Upon cooling, the χT product remains roughly constant down to 50 K. Below 50 K,

Table 2. Selected Bond Distances for $[Ru^{II}(NH_3)_2(bqdi)Cl_2]$ (I),[a] and Species II and IIIc

	Bond Distances (Å)		
	I	II	IIIc
Ru−N1	1.969(3)	1.985(5)	2.084(3), 2.097(3) (N1,N2)
Ru−N2	2.149(3)	2.135(6)	2.116(3), 2.110(3) (N3,N4)
Ru−Cl2	2.373(1)	2.313(3)	2.3358(9)
Ru−Cl1	2.382(1)	2.352(2)	2.3406(9)
N1−C1	1.330(5)	1.323(8)	1.462(5), 1.447(5) (N1−C1, N2−C2)
C1−C2	1.408(5)	1.424(9)	1.378(6), 1.392(5) (C1−C6, C2−C3)
C1−C1A	1.457(7)	1.443(9)	1.381(6) (C1−C2)
C2−C3	1.358(6)	1.357(9)	1.378(6), 1.376(6) (C3−C4, C5−C6)
C3−C3A	1.427(8)	1.445(9)	1.384(6) (C4−C5)

[a] Data taken from ref 23.

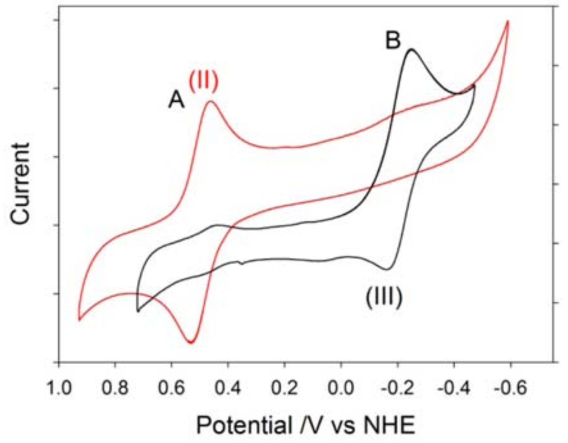

Figure 4. Cyclic voltammograms of species $[Ru^{III}(NH_3)_2(bqdi)Cl_2]Cl$ (**II**) (red trace) and $[Ru^{III}(NH_3)_2(opda)Cl_2]Cl$ (**III**) (black trace) in methanol/TBAPF$_6$. Scan rate = 100 mV s^{-1}.

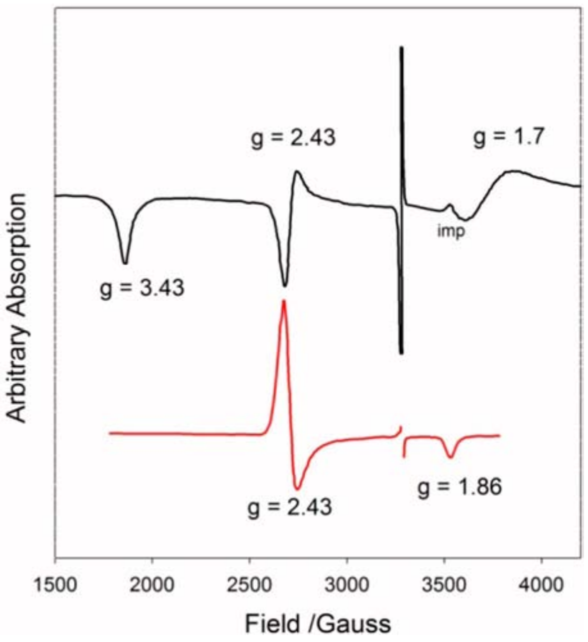

Figure 5. Electron paramagnetic resonance (EPR) spectra of species **II** (lower, red trace) and **III** (upper, black trace), both in frozen methanol, at liquid nitrogen temperature. The DPPH signal is shown for the species **III** trace and has been mostly excluded for the species **II** trace. No signals were observed for species **II** below 2000 G.

χT decreases rapidly to reach a minimum value of 0.11 cm^3 K mol^{-1} at 2 K. This decrease is most likely due to a combination of factors, such as significant magnetic anisotropy and/or weak intermolecular antiferromagnetic interactions. The data could be fitted to the Curie−Weiss law ($C = 0.46$ cm^3 K mol^{-1} and $\theta = -4.20$ K), which suggests a weak intermolecular antiferromagnetic interaction. It was not possible to obtain a sufficiently dry and pure (removal of solvent caused some slight decomposition) sample of species **III** to pursue its magnetism.

Electron Paramagnetic Resonance (EPR) Spectra. The EPR spectra of ruthenium complexes of quinonoid ligands have been extensively studied and most frequently involve semiquinones. These species usually give rise to anisotropic spectra with *g*-values clustered close[30−37] to 2.0. Ruthenium(III) complexes containing the closed-shell quinone are rare, but one is reported[37] to give a slightly rhombically split, axial signal. Ruthenium(III) complexes containing the fully reduced catecholate are quite common and usually give rise to an anisotropic signature (see, e.g., refs 32 and 37−39). Generally, ruthenium(III) species in pseudo-octahedral environments may have rhombic or axial symmetry.[40] Indeed, the species **II** spectrum appears axial while species **III** exhibits a rather typical rhombic low spin d^5 Ru^{III} spectrum (see Figure 5).

As further confirmation, the *g*-tensors were evaluated using DFT and the NMR keyword. The results are approximate and the numerical values are dependent, to some degree, on the basis set used; however, it is satisfying that these calculations confirm the above analysis. Thus, using B3LYP (PCM, methanol), the *g*-tensors evaluated for these species are

Species **II**: 2.27, 2.27, 2.02 (axial, C$_s$)
Species **III**: 2.82, 2.38, 2.00 (rhombic, C$_2$)

which is in excellent agreement with the experimental pattern and is in moderate agreement with the numerical values. Thus, the unpaired electron in species **III** clearly displays a rhombic signal, while that of species **II** is tetragonal (see DFT discussion below).

Density Functional Theory (DFT) Calculations. The DFT analysis initially employed the B3LYP functional and LANL2DZ basis sets, which work well with many ruthenium species but have a tendency to overestimate some metal−ligand distances.[41−51] In this system, the Ru−Cl distance was especially overestimated. To alleviate this error, we explored using triple-ζ functions, initially trying def2-TZVP for ruthenium[52] while retaining LANL2DZ for the other elements. This improved the situation (Table 3) but the Ru−Cl bond was still rather too long. However, including def2-TZVP for both

Table 3. Comparative Selected Bond Distances with Basis Set, DFT[a]

bond	LANL2DZ – C,H,N,Cl,Ru	LANL2DZ – C,H,N,Cl; def2-TZVP Ru	LANL2DZ – C,H,N; def2-TZVP Ru, Cl [X-ray expt]
$[Ru^{III}(NH_3)_2(bqdi)Cl_2]^+$ (**II**)			
Ru–NH_3	2.16	2.15	2.16 [2.135]
Ru–N_{bqdi}	2.01	1.985	1.985 [1.985]
Ru–Cl	2.43	2.40	2.35 [2.33_{av}]
C=NH	1.33	1.34	1.34 [1.32]
$[Ru^{II}(NH_3)_2(bqdi)Cl_2]$ (**I**)[b]			
Ru–NH_3	2.18	2.16	2.17 [2.15][b]
Ru–N_{bqdi}	2.00	1.98	1.98 [1.97]
Ru–Cl	2.50	2.47	2.41 [2.38]
C=NH	1.35	1.355	1.355 [1.33]
$[Ru^{III}(NH_3)_2(opda)Cl_2]^+$ (**III**)			
Ru–NH_3	2.15	2.14	2.14 [2.12]
Ru–N_{opda}	2.14	2.12	2.13 [2.08]
Ru–Cl	2.43	2.41	2.36 [2.34]
C–NH_2	1.47	1.48	1.48 [1.46]

[a] Experimental values given in square brackets. [b] Experimental data previously reported in ref 23.

chlorine and ruthenium led to excellent agreement between predicted DFT key bond distances and X-ray data for species **II** and **III** and very good agreement for species **I** (see Table 3). Employing def2-TZVP for anionic ligands is especially effective.

Therefore, we employed LANL2DZ for C, H, and N, and def2-TZVP for Ru and Cl. The computation employs a geometry-optimized molecule in a PCM (methanol) in silico environment.

Both species could belong to point groups C_1, C_2, C_s, or C_{2v}, depending on the relative orientations of the ammine protons. Not unexpectedly, these alternatives have very similar SCF energies; indeed, in solution, the ammine groups are likely rotating. We initially chose to use the C_{2v} orientation for both species to maximize symmetry, since this also corresponds to the molecular symmetry of species **II** in the crystal. However, this led to some negative frequencies in the vibrational spectrum associated with ammine group rotation. Indeed, a small rotation of the ammine groups and C_s symmetry removed the negative frequencies for species **II** (the mirror plane bisects the bqdi ring and the two Ru-NH_3 bonds), while C_2 symmetry removed the negative frequencies for species **III**. In the X-ray structure of species **III**, the opda group is slightly canted out of the N_4 plane, as noted above, but in the geometry-optimized C_2 version, the opda lies in the N_4 molecular plane.

Molecular Orbitals of $[Ru^{III}(NH_3)_2(bqdi)Cl_2]Cl$ (II). Figure 6 shows the makeup of the frontier α- and β-manifold orbitals of species **II**. We assume a 2-fold (z-) axis through the bqdi ligand with the bqdi plane being xz. The α-#63 orbital (HOMO) is mostly comprised of π-bqdi (HOFO, highest occupied fragment orbital) in an out-of-phase (antibonding) combination with the Ru d_{xy} orbital that has δ-symmetry (Figure 7 (left)), with respect to the bqdi ligand ($d\delta$). Orbital α-#61 is the corresponding in-phase (bonding) combination, and α-#55 is d_{xy} bonding to π-chloride. Orbitals α-#56 and α-#62 involve a bonding and antibonding interaction of d_{yz} and π-chloride, respectively. α-#62 is also bonding between d_{yz} and π^*-LUFO (bqdi) (lowest unoccupied fragment orbital).

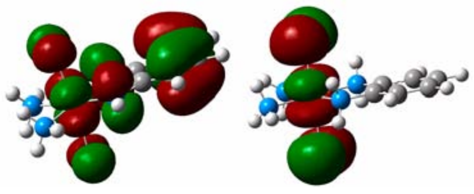

Figure 7. Location of unpaired α-electron in (left) species **II** (α-#63, HOMO) and (right) species **III** (α-#63, HOMO-1).

The LUMO (α-#64) comprises the antibonding d_{yz}–π-bqdi combination. The relatively pure d-orbital (MO α-#60) is d_{xz} that lies in the bqdi molecular plane. It has a weak σ-interaction with bqdi and an antibonding interaction with to π-chloride.

The empty β-#63 orbital is mostly d_{xy}, so the "hole" in this low-spin d^5 complex (**II**) lies on d_{xy}, and the odd electron is in the α-#63 orbital (overlap 0.76 with β-#63). The two orbitals, d_{xy} and d_{yz} (HOMO and HOMO-1), differ in energy by 0.12 eV and therefore are fairly close to an "e" pair, displaying pseudo-tetragonal symmetry (see EPR above).[53] Orbital β-#62 corresponds with α-#62 as a π-bonding combination between d_{yz} and π^*-LUFO (bqdi). Similarly, β-#60 is the partner of α-#60.

Table 4 lists some of the electronic structural characteristics of the $[Ru^{III}(NH_3)_2(bqdi)Cl_2]^+$ species (**II**) derived with this

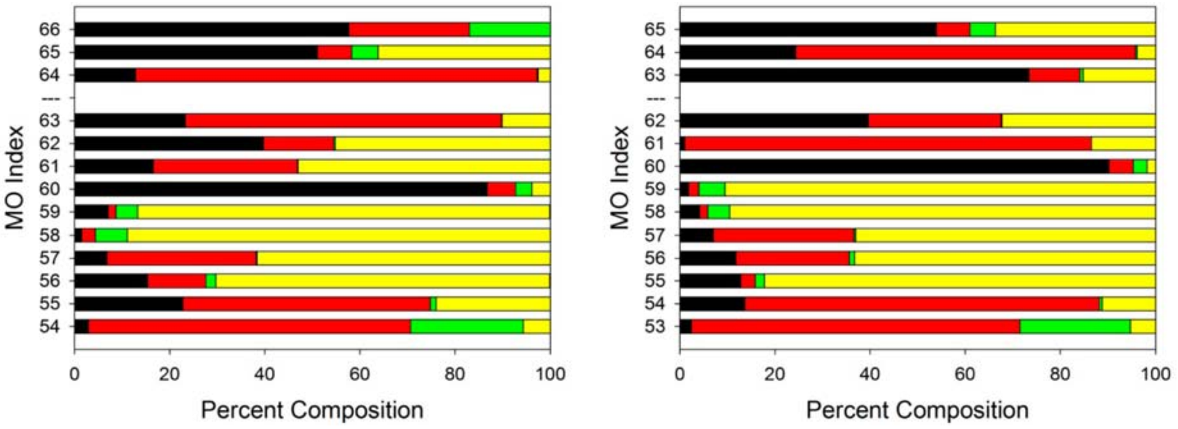

Figure 6. Percent composition of frontier orbitals of $[Ru^{III}(NH_3)_2(bqdi)Cl_2]Cl$ (**II**) (left-α, right-β). Legend: Ru (black), bqdi (red), chloride (yellow), ammonia (green). DFT (B3LYP LANL2DZ and def2-TZVP, PCM methanol (see text)). The HOMO–LUMO gap is represented by the larger white bar identified by "---" along the vertical axis to the left of each panel.

Table 4. Summary of Charges, Spin Densities, and Bond Orders for $[Ru^{III}(NH_3)_2(bqdi)Cl_2]^+$ (**II**) and the Parent Species $[Ru^{II}(NH_3)_2(bqdi)Cl_2]$ (**I**)

	$[Ru^{III}(NH_3)_2(bqdi)Cl_2]^+$ (**II**)	$[Ru^{II}(NH_3)_2(bqdi)Cl_2]$[a] (**I**)
net Mulliken (NPA)[b] charge on Ru	+0.88 (+0.10)	+0.86 (+0.00)
net Mulliken (NPA) charge on $[Ru(NH_3)_2Cl_2]$	+0.63 (+0.37)	+0.15 (−0.14)
net Mulliken (NPA) charge on bqdi	+0.37 (+0.63)	−0.15 (+0.14)
σ,π-transfer bqdi → Ru	0.39(α), 1.13(β)[c]	0.69
π-transfer Ru → bqdi	0.18(α), 0.32(β)[c]	0.85
occupancy #29 bqdi	0.14(α), 0.25(β)	0.73
$[Ru(NH_3)_2Cl_2]$ [bqdi] bond order	0.86(α), 1.13(β)	2.15
Ru−NH(bqdi) bond order	0.74(α), 1.00(β)[d]	1.56[d]
Ru−NH_3 bond order[c]	0.44(α), 0.42(β)[d]	0.66[d]
Ru−Cl bond order[c]	0.72(α), 0.93(β)[d]	1.31[d]
net spin on Ru−Mulliken (NPA)	0.96 (0.87)	n.r.[e]

[a] For direct comparison, these data were derived using Gaussian 09 C.01, LANL2DZ, and def2-TZVP, as noted in the text, and the PCM model with methanol as the solvent; therefore, the data differ slightly from those reported in the earlier paper.[23] [b] Natural population analysis. [c] Large electronic (β) polarization $[Ru(NH_3)_2Cl_2]$ − (bqdi) = 0.76 a.u. [d] Per two ligands. [e] n.r. = not relevant.

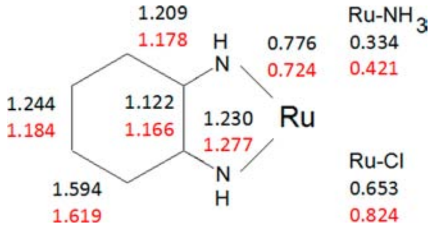

Figure 8. Comparison of Mayer bond orders in species **I** and **II**. The black data refer to the ruthenium(II) species, and the red data refers to the ruthenium(III) species. The molecule has C_s symmetry with the mirror plane bisecting the bqdi ring, so the C_s symmetry-related bonds have the same force constants, which, therefore, are not shown.

computational analysis. More subtly, the Ru-NH(bqdi) and the $[Ru(NH_3)_2Cl_2]$ and [bqdi] fragment bond orders are larger from the β-manifold than from the α-manifold, because the extra α-electron is in an orbital that is antibonding with respect to bqdi. The greater donation from bqdi to Ru^{III} in the β-manifold than the α-manifold, while incorporating a polarization contribution is also real because the "hole" in the β-manifold allows π-donation from bqdi to Ru^{III}, which is not possible in the α-manifold.

The α-#61 orbital is antibonding between d_{xy} and a pair of chloride π-orbitals. Since the β-d_{xy} electron is absent, there is no such antibonding interaction in the β-manifold, thereby explaining why the β-Ru−Cl bond order exceeds that of the α-Ru−Cl bond order. The d_{xy} orbital does not interact with the ammonia residues, so the Ru−NH_3 bond orders are the same in both manifolds.

It is of interest to include herein a comparison with the corresponding ruthenium(II) species $[Ru^{II}(NH_3)_2(bqdi)Cl_2]$ (**I**). Species **I** is unusual in having very strong π-back-donation from Ru to bqdi, such that the overall net charge on the bqdi fragment is negative, despite the σ-bonding interaction, which would move charge toward Ru. This π-back-donation is greatly diminished in species **II**, because of the higher formal charge on Ru. Hence, the net charge on bqdi is now ca. 0.52 a.u. more positive than in species **I**. The net positive charge on the molecular fragment $[Ru(NH_3)_2Cl_2]$ is correspondingly much greater in **II** than in **I**. The bond order between the $[Ru(NH_3)_2Cl_2]$ and [bqdi] fragments is smaller for the Ru^{III} species (total 1.99) than for the Ru^{II} species (2.15), because of the enhanced π-back-donation in the latter. The individual Ru−N bonds (Figure 8) also have higher bond orders for the Ru^{II} species than for Ru^{III}. Both the Ru−NH_3 and Ru−Cl bond orders, on the other hand, are greater for the Ru^{III} than the Ru^{II} species, which is due to the greater positive charge on the former. The variations in the bqdi bond orders (Figure 8) reveal that the bqdi ligand is more quinonoid in the Ru^{III} than in the Ru^{II} species, where the quinonoid character is reduced significantly by the π-back-donation.

Molecular Orbitals of $[Ru^{III}(NH_3)_2(opda)Cl_2]Cl$ (III). The frontier molecular orbital composition is displayed in Figure 9. Since there is only a σ-interaction with the opda ligand, π-MOs associated with this ligand are essentially pure with little mixing with metal, ammonia, or chloride (see, e.g., α,β-#60,61). The α,β-#62 MOs are clearly d_{xz} lying in the opda molecular plane and, lacking interaction with chloride, are essentially pure d-orbitals. As in species **II**, the "hole" is in a d_{xy}-orbital, but here the "odd" α-d_{xy} is the HOMO-1, although still α-#63. Thus, α-#55,56 and α-#63,64 comprise the bonding and antibonding combinations between d_{xy} and d_{yz} and π-chloride, respectively. The absence of an electron in β-d_{xy} explains the absence of the aforementioned pair of bonding and antibonding combinations with π-chloride in the β-manifold.

The unpaired α-electron resides in HOMO-1 (α-#63), which overlaps the β-LUMO (#64) with an overlap integral of 0.90. HOMO-1 is close in energy with HOMO-2 (differ by 0.1 eV), so the unpaired electron again resides in a quasi-tetragonal environment; however, in this case, we observe a rhombic EPR spectrum. Species **III** possesses a very low-lying d−d excited state (at ca. 2100 cm^{-1}) in which the odd electron is now in d_{yz}; this will provide a mixing mechanism[54] to generate the rhombic asymmetry of the EPR spectrum. In species **II**, such d−d excited states lie at or above 6500 cm^{-1} (see Tables S4 and S6 in the Supporting Information), therefore, species **II** exhibits a tetragonal EPR spectrum.

Electronic Spectra. Figures 10 and 11, and Table 5, display the experimental spectra of species **II** and **III** and the TD-DFT predicted spectra (also see Tables S4 and S6 in the Supporting Information). The TD-DFT analysis of species **II** reproduces the visible region band envelope of a strong band (labeled "9") with its two nearby lower (labeled "6,7") and higher (labeled "13") energy satellites extremely well. The energy of the experimental band at 21 050 cm^{-1} is predicted exactly, and the predicted satellite energies also agree well. The intense transition (labeled as "9" in Figure 10) is very complex, being a mixture of $L_{Cl}L_{bq}CT$, chloride to π^* bqdi charge transfer, $L_{bq}MCT$, bqdi π → Ru 4dπ to the hole in the β-manifold, and indeed MLCT to π^* bqdi in the α-manifold. A predicted transition 10, π−π^* bqdi, apparently lies under the broad envelope of this intense transition. The peak at 16 660 cm^{-1} is assigned to the transitions labeled "6,7", a similar complex combination of transitions (see Table 5). The experimental band near 25 000 cm^{-1} is evidently the expected $L_{Cl}MCT$, chloride to the hole on the metal CT. The UV absorption arises from many transitions contributing to the broad experimental band between 30 000 cm^{-1} and 35 000 cm^{-1}. However, TD-

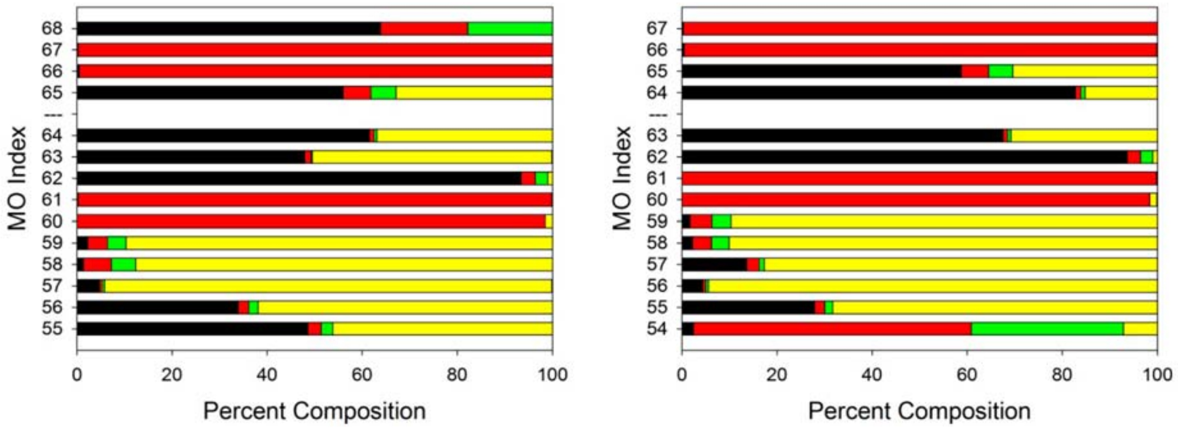

Figure 9. Percent composition of frontier orbitals of $[Ru^{III}(NH_3)_2(opda)Cl_2]Cl$ (**III**) (left, α; right, β). Legend: Ru (black), opda (red), chloride (yellow), and ammonia (green). (B3LYP LANL2DZ and def2-TZVP, PCM water (see text).)

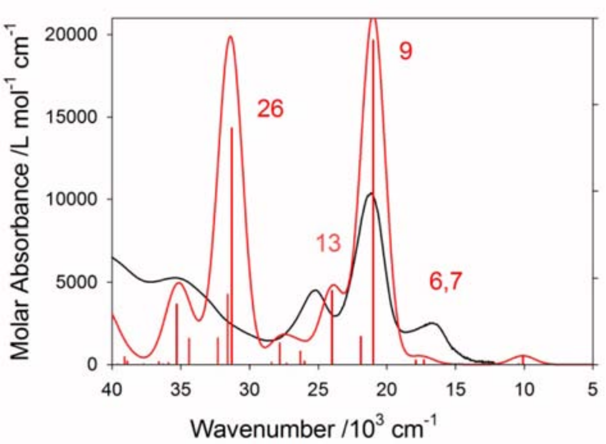

Figure 10. Electronic spectra of $[Ru^{III}(NH_3)_2(bqdi)Cl_2]^+$ (**II**). Time-dependent DFT spectrum of solvent (methanol) optimized geometry (red). Experimental spectrum in methanol (black). The numbering of key bands refers to the numerical listing given in the Supporting Information and Table 5.

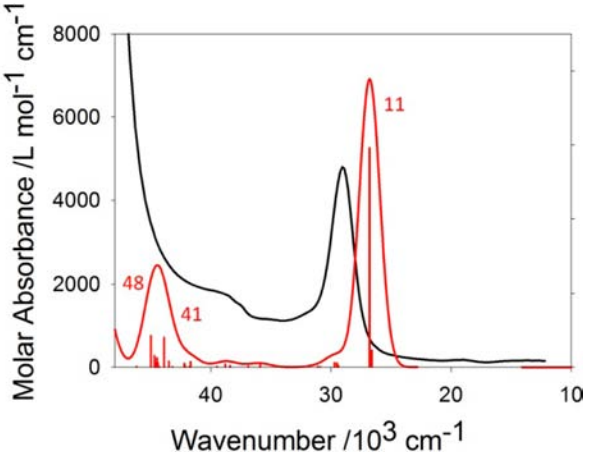

Figure 11. Electronic spectra of $[Ru^{III}(NH_3)_2(opda)Cl_2]^+$ (**III**). Experimental spectrum in dilute aqueous HCl (black trace); DFT predicted spectrum of the aqueous-phase optimized geometry (red trace).

DFT seriously overestimates the intensity of the transition labeled “26”.

Interestingly, species $[Ru^{III}(NH_3)_2(opda)Cl_2]^+$ (**III**) has just one strong, narrow, absorption in the near-UV region (28 900 cm^{-1}), with a significant shoulder near 39 000 cm^{-1}, rising to a very intense absorption at ca. 50 000 cm^{-1} (see Figure 11).

Since the π-levels of opda are not conjugated with ruthenium, the electronic spectrum of species **III** is expected[52] to be much simpler than that of species **II**. The only low-energy transition with significant intensity is peak 11, which is the anticipated $L_{Cl}MCT$ transition, from chloride to the hole in Ru $d\pi^5$ (see Table 5). The shoulder near 39 000 cm^{-1} is the other expected LMCT transition, $L_{op}MCT$, while the band near 50 000 cm^{-1} is due to a cluster of internal opda $\pi-\pi^*$ transitions. Aside from the near-UV band, the predicted spectrum shows no strong transitions below ca. 50 000 cm^{-1} (see Table 5 and Table S6 in the Supporting Information).

There has been some discussion of the use of TD-DFT, as currently formulated,[55] for open-shell calculations, specifically that it cannot deal with them properly.[56] However, the agreement here is quite acceptable, aside from one rather too-intense transition. We have previously seen very good agreement between theory and experiment for open-shell species[41] including higher-energy transitions (at least to 40 000 cm^{-1}).

Resonance Raman (RR) Spectroscopy. The resonance Raman (RR) spectra of $[Ru^{III}(NH_3)_2(bqdi)Cl_2]^+$ (**II**) excited at 488 and 782 nm are shown in Figure 12, together, for comparison purposes, with that of the previously reported[23,57] $[Ru^{II}(NH_3)_2(bqdi)Cl_2]^+$ (**I**). Weak overtone and combination bands are also observed (see Figure S3 in the Supporting Information), but they are not as well-defined as was previously obtained with the parent species (**I**) and are not discussed further. The DFT-calculated Raman spectrum of $[Ru^{III}(NH_3)_2(bqdi)Cl_2]^+$ (**II**) is also included. This calculation requires an energy-minimized structure and the gas-phase optimized geometry was used. Three strong bands in the 1400−1500 cm^{-1} region are clearly associated with the three experimental bands in this region. The calculated wavenumber data were multiplied by a factor of 0.96 to map onto the experimental data. Overall agreement in energy between the observed and calculated (scaled) data is remarkably good. The most obvious difference is the weakness of the bands below 1200 cm^{-1}, relative to those near 1500 cm^{-1}, in the regular (nonenhanced) Raman spectrum (see the top panel in Figure 12).

Table 5. Comparison of Experimental and DFT Calculated Optical Spectra and Assignments[a]

#[b]	Observed (cm^{-1})	Observed ε (L mol^{-1}cm^{-1})	Calculated (cm^{-1})	Calculated oscillator strength, f	assignment[c]
					[Ru^{III}(NH$_3$)$_2$(bqdi)Cl$_2$]$^+$ (II) (C_s symmetry)
1			6500	0.000	60 →63β(98%) d−d
2			6500	0.000	62 → 63β(95%) d−d
3			10100	0.0045	62 → 64β (61%), 62 → 64α(39%) ML$_{bq}$CT, L$_{Cl}$L$_{bq}$CT
4			10400	0.0005	63 → 64α (66%), 61 → 64β(29%) π−π* bqdi
6	16660	2820	17300	0.003	61 → 63β(59%), 62 → 64α(26%) L$_{bq}$MCT, ML$_{bq}$CT, L$_{Cl}$L$_{bq}$CT
7			17900	0.0025	61 → 64α(49%), 61→ 64β(24%) L$_{Cl}$L$_{bq}$CT, π−π* bqdi
9	21050	10900	21000	0.187	61 → 63β(38%), 62 → 64α(33%), 62 → 64β(23%) L$_{bq}$MCT, L$_{Cl}$L$_{bq}$CT, ML$_{bq}$CT
10			21900	0.016	61 → 64α(45%), 61 → 64β(44%) L$_{Cl}$L$_{bq}$CT, π−π* bqdi
13	25250	3250	24000	0.043	59 → 63β(95%) L$_{Cl}$MCT
26	35500	br	31300	0.136	57 → 64α(33%), 57 → 64β(24%) L$_{Cl}$L$_{bq}$CT
28			31600	0.040	60 → 65α(37%), 60 → 65β(26%) d−d
34			35300	0.035	v. mixed
					[Ru^{III}(NH$_3$)$_2$(opda)Cl$_2$]$^+$ (III)
1			2100	0.000	63 → 64β(97%) d−d
11	28900	5230	26800	0.059	59 → 64β(98%) L$_{Cl}$MCT
26	38460	sh,br	38800 etc.[e]	0.0008	54 → 64β(96%) L$_{op}$MCT, etc.[d]

[a] Additional theoretical predictions can be found in Tables S4 and S6 in the Supporting Information. [b] Transition number as listed in the Supporting Information. [c] L$_{Cl}$L$_{bq}$CT refers to chloride-to-bqdi charge transfer, ML$_{bq}$CT refers to ruthenium-to-bqdi charge transfer, L$_{Cl}$MCT refers to chloride-to-ruthenium charge transfer, and L$_{op}$MCT refers to opda-to-ruthenium charge transfer. [d] One of a group of closely spaced, weak, transitions.

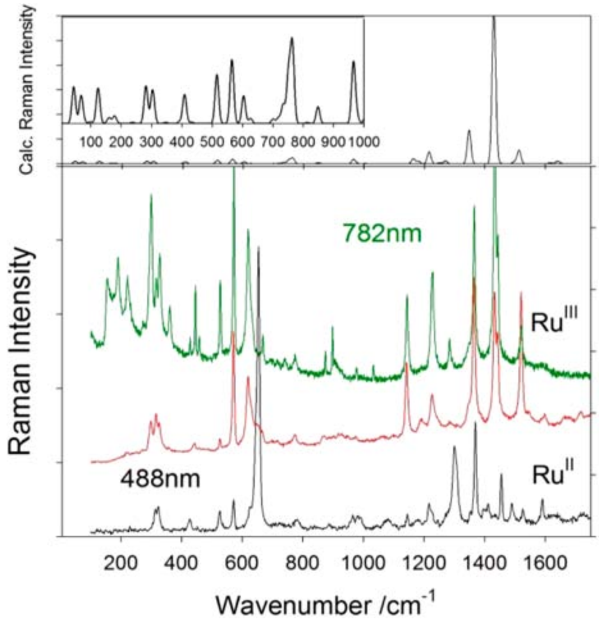

Figure 12. Resonance Raman (RR) spectra of [Ru^{II}(NH$_3$)$_2$(bqdi)Cl$_2$] (I) (black trace) and [Ru^{III}(NH$_3$)$_2$(bqdi)Cl$_2$]$^+$ (II) (red trace), both excited at 488 nm, [Ru^{III}(NH$_3$)$_2$(bqdi)Cl$_2$]$^+$ (II) excited at 782 nm (green trace); the DFT-calculated Raman spectrum of [Ru^{III}(NH$_3$)$_2$(bqdi)Cl$_2$]$^+$ (II) with methanol solvent optimized geometry (B3LYP/LANL2DZ) (see text) is shown at the top of the main panel. The inset in the top panel is the region from ~0 to 1000 cm^{-1}, scaled up by a factor of 20. DFT-calculated wavenumbers are shifted down by a factor of 0.96.

A key difference between the 488-nm and 782-nm RR spectra is the enhancement of low-energy vibrations near 200−300 cm^{-1} in the 782-nm spectrum, relative to the 488-nm spectrum. We expect that the 782-nm excitation will enhance vibrations involved with the weak L$_{Cl}$MCT and LLCT transitions (Table 5). Therefore, we assign the transitions in this 200−300 cm^{-1} region to Ru−Cl modes, as confirmed by the DFT analysis, which shows the symmetric and asymmetric Ru−Cl stretching modes to lie at 281 and 347 cm^{-1}, respectively (0.96 correction included).

The visible region electronic absorption involves the π and π* orbitals of the bqdi ring (Table 5) and three strongly enhanced vibrations are observed at 1400−1500 cm^{-1} associated, according to the DFT analysis, with bqdi ring breathing modes coupled to NH(bqdi) deformation modes (also see ref 57). There are also several ammonia deformation modes in this general region, the most intense of which, according to DFT, lies at 1665 cm^{-1} (corrected). There is no trace of this vibration in the RR spectrum, and the DFT analysis reveals that these ammonia modes are essentially uncoupled from the bqdi breathing modes. Thus, we conclude that all three enhanced modes in the 1400−1500 cm^{-1} region are bqdi ring breathing modes.

Charge transfer excitation from, or to, ruthenium, necessarily changes the electron density on the metal and, hence, will excite Ru−N modes. These modes are coupled to ring breathing modes of the ruthenium bqdi metallocycle and are enhanced in the 500−600 cm^{-1} region of both sets of RR spectra. As noted above, extensive π-back bonding in the parent species (I) causes extensive mixing between the ground state and the excited state and is recognized by the much greater intensity of the enhanced metallocycle ring breathing mode (ca. 600 cm^{-1}), relative to the bqdi breathing modes. This is discussed in depth elsewhere.[23,57] The discussion regarding Table 4 above shows that this mixing is much less effective in species II, and this is nicely illustrated by the comparable intensities of the metallocycle and bqdi breathing modes in the RR spectra of this species (II). The most intense vibration in this region lies at 573 cm^{-1} (DFT, corrected; 564 cm^{-1} Expt.), which is the symmetric Ru−N(H) stretching mode obviously strongly coupled to a symmetric metallocycle breathing mode. Although this species contains Ru^{III}, this vibration lies considerably below the corresponding vibration in the Ru^{II} species (I) at 654 cm^{-1}, where the bonding is strongly enhanced by π-back-donation. Thus, the RR data elegantly support both the electronic spectrum assignments and the theoretical analysis of the electronic structure.

Mechanism of Disproportionation. There are no basic lone pairs on the parent species (**I**), so it is curious that it should so readily react with acid.

Keene and Meyer[58] reported an electrochemical oxidation of ruthenium-bound ethylenediamine to form a diimine involving *a four-electron oxidation with the loss of four protons*. Our process, while involving two electrons (because the ligand is already partly unsaturated), is basically similar but in reverse: *a two-electron reduction with a gain of two protons*. A similar type of mechanism may operate here. In the Meyer mechanism, $[\mathrm{Ru^{II}(bpy)_2(en)}]^{2+}$ is electrochemically or chemically (Ce(IV)) oxidized to $[\mathrm{Ru^{III}(bpy)_2(en)}]^{3+}$. Two $[\mathrm{Ru^{III}(bpy)_2(en)}]^{3+}$ molecules then facilitate a two-electron oxidation of one molecule as follows:

$$\begin{aligned}&2[\mathrm{Ru^{III}(bpy)_2(en)}]^{3+}\\&\quad\rightarrow [\mathrm{Ru^{II}(bpy)_2(en)}]^{2+} + [\mathrm{Ru^{II}(bpy)_2(monoim\text{-}en)}]^{2+}\\&\qquad + 2\mathrm{H}^+\end{aligned} \tag{2}$$

where, in (monoim-en), one $\mathrm{CH_2{-}NH_2}$ has been oxidized to CH=NH. A second analogous step then proceeds to form the diimine. Reaction 2 may be thought of as starting with two Ru(III) species that lead to two products: one with a net-one-electron reduction (left, $\mathrm{Ru^{II}}$ species) and one with a net-one-electron oxidation (right, $\mathrm{Ru^{II}}$ monoim-en) species.

$$\begin{aligned}&\underset{(\mathbf{I})}{\mathrm{Ru^{II}(NH_3)_2(bqdi)Cl_2}}\\&\quad + 2\mathrm{H}^+ \rightarrow \underset{(\mathbf{IV})}{[\mathrm{Ru^{IV}(NH_3)_2(opda)Cl_2}]^{2+}}\end{aligned} \tag{3}$$

$$\begin{aligned}&\underset{(\mathbf{IV})}{[\mathrm{Ru^{IV}(NH_3)_2(opda)Cl_2}]^{2+}} + \underset{(\mathbf{I})}{\mathrm{Ru^{II}(NH_3)_2(bqdi)Cl_2}}\\&\quad\rightarrow \underset{(\mathbf{III})}{[\mathrm{Ru^{III}(NH_3)_2(opda)Cl_2}]^{+}}\\&\qquad + \underset{(\mathbf{II})}{[\mathrm{Ru^{III}(NH_3)_2(bqdi)Cl_2}]^{+}}\end{aligned} \tag{4}$$

The thermodynamics of eq 1 can be assessed via reactions 3 and 4, even if, as is likely, species IV is ephemeral. These reactions sum to eq 1. Reaction 3, as a gas phase protonation process, is downhill and reaction 4 is an isodesmic reaction[59] which is also thermodynamically downhill. The relevant free energies are shown in Table 6. Indeed, the disproportionation process, in eq 1, is thermodynamically downhill.

It is useful in our case to recall that $\mathrm{Ru^{III}(NH_3)_2(sqdi)Cl_2}$, where sqdi = benzosemiquinonediiminato(1-), is a resonance contributor to species **I**, because of the extensive π-back-donation therein. This resonance form moves more charge to the coordinating nitrogen atoms, which may then facilitate a reaction with protons to form a putative protonated reactive intermediate, $[\mathrm{Ru(NH_3)_2(bqdi\text{-}H^+)Cl_2}]^+$ (**V**), which will be an excellent oxidant. This oxidant then abstracts an electron and a proton from another molecule of **I**, resulting in a proton-coupled disproportionation of two molecules of **I** to yield the products **II** and **III**.

Table 6. Isodesmic Calculation of eq 4 (Gas Phase) (via DFT; C,H,N LANL2DZ; and Ru,Cl def2-TZVP)

species	SCF energy (Hartrees)
I	−1470.400687
II	−1470.175829
III	−1471.410188
IV[a]	−1471.010674
IV + **I**	−2941.411361
II + **III**	−2941.586018
ΔG	−0.175[b]

[a]Spin triplet. [b]Equal to −459 kJ/mol.

The formation of the protonated intermediate (**V**) must involve some internal redistribution of electron density, since there is no site on benzoquinonediimine to accept a proton. A DFT geometry-optimized structure for this species (**V**) reveals it to be best-described as $[\mathrm{Ru^{III}(NH_3)_2(sqdi\text{-}H)Cl_2}]^+$. It is a species that contains $\mathrm{Ru^{III}}$ strongly spin-coupled to the protonated diiminosemiquinone (sqdi-H), being the neutral 1-amino-2-iminosemiquinone. The Ru-$\mathrm{NH_2}$(sqdi-H) and Ru-NH(sqdi-H) bond lengths are calculated as 2.14 and 1.86 Å, respectively.

Species **IV** was also geometry-optimized. It can exist as a spin singlet or triplet, the latter being favored by 0.03 hartree in the gas-phase DFT calculation. It is, of course, the singly oxidized product of species **III**, and its geometry is quite similar thereto. The major difference is a much shorter Ru−Cl bond length of 2.25 Å; the four Ru−N distances are essentially the same as those in species **III**.

Some effort was expended to determine if there were any intermediates in this reaction that could be trapped at low temperature. At the freezing temperature of water, the reaction slowed but no additional species were evident. Note, in passing, that the related species[60] $[\mathrm{Ru^{II}(acac)_2(bqdi)}]$ does not respond to acid in this fashion.

Aspects of Reactivity. The relative intensities of the 28 900 cm^{-1} absorption band (**III**, Figure 1) and the 21 050 cm^{-1} absorption band (**II**, Figure 1) varied somewhat in different experiments, depending on the solvent, the presence of oxygen or argon, the time, and the pH. The chemical interconversions between the various species are summarized in Figure 13. The fundamental chemistry has been discussed above. Furthermore, we note that if a disproportionated solution containing both species **II** and **III** is left to stand in an inert gas atmosphere under acidic conditions, then the peaks due to [Ru-

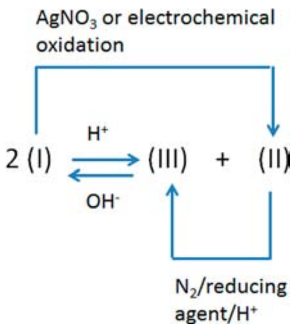

Figure 13. Reactivity of species **I**, **II**, and **III**. $\mathrm{Ru(NH_3)_2(bqdi)Cl_2}$ (**I**) is converted to $[\mathrm{Ru(NH_3)_2(bqdi)Cl_2}]^+$ (**II**) with a chemical oxidant, such as $\mathrm{AgNO_3}$, or by controlled potential oxidation. Species **II** is converted to species $[\mathrm{Ru(NH_3)_2(opda)Cl_2}]^+$ (**III**) (two-electron reduction) in an acidic medium in the presence of an expeditious or deliberately added reducing agent.

$(NH_3)_2(bqdi)Cl_2]^+$ (**II**) slowly diminish in intensity while those for species $[Ru(NH_3)_2(opda)Cl_2]^+$ (**III**) grow larger; thus, species **II** is being converted to species **III**, which is a two-electron reduction process. The reaction is more rapid and goes to completion (species **III**), if a reducing agent such as sodium hypophosphite is added (Figure 13). This can be understood as follows: species **II**, in the presence of acid, is a moderately strong oxidant and will oxidize expeditious reductants or deliberately added reductant (e.g., hypophosphite). This will generate the initial Ru^{II} species (**I**). Since acid is present, this will disproportionate back to **II** and **III**. However, this represents a net conversion of two molecules of **II** to form **II** + **III**, and thus species **II** will ultimately be converted entirely to species **III**.

Both species **II** and **III**, if left in neutral water in air, will ultimately decay back to species **I** (the latter more rapidly (within minutes) than the former). Since no acid is present, there will be no subsequent disproportionation. Species **II** is stable on a time scale of days in dilute acid solutions, such as 1 M HCl.

$[Ru^{III}(opda)(NH_3)_2Cl_2]^+$ (**III**) converts back instantly to the parent (**I**) when treated with a base in air, because deprotonation will create, at least transiently, the $[Ru^{II}(NH_3)_2(sqdi)Cl_2]^-$ species that will be sensitive to air; the reaction is much slower under inert gas (i.e., reoxidation is suppressed). $[Ru^{III}(bqdi)(NH_3)_2Cl_2]^+$ (**II**) also converts back rapidly to the parent (**I**) when treated with NaOH, under argon or air, probably because the hydroxide ion behaves as a reductant (see Figure 14).[61,62]

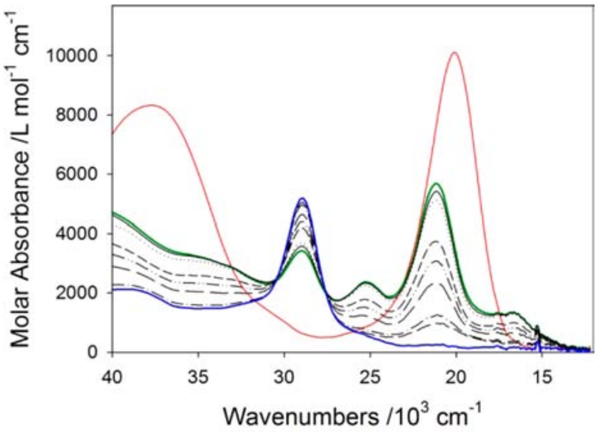

Figure 14. The initial solution of $Ru^{II}(NH_3)_2(opda)Cl_2$ (**I**) (red trace), in methanol, treated with HCl, disproportionates, yielding a mixture of species **II** and **III** (green trace). Upon the addition of sodium hypophosphite under argon, species **II** converts, over a period of hours, to $[Ru^{III}(NH_3)_2(opda)Cl_2]^+$ (**III**) (blue trace). Note the isosbestic points at 30 440 and 27 570 cm^{-1}.

Some Consideration of Isosbestic Points. In Figure 1, we see isosbestic points with apparently three species in equilibrium. As noted by Drago,[24] this is certainly possible; however, in this case, while three species are indeed involved, it is a special case of two species in equilibrium. Thus, species **I** is converted to a 50:50 mix of **II** and **III**. Over the short time of the experiment, we can assume that there is little or no subsequent conversion of **III** to **II** in air. This 50:50 mixture has a specific electronic spectrum, being the sum of the spectroscopic signatures of species **II** and **III**, the sum of which may be considered that of a single species. Thus, the isosbestic is formed, as a two-component equilibrium, between the spectrum of **I** and the spectrum of this mixture of **II** + **III**.

In Figure 2, we have a different set of isosbestic points for the conversion of **I** directly to **II**, while in Figure 14, there is yet another set for the conversion of **III** to **II**.

CONCLUSION

A proton-induced disproportionation is introduced and analyzed in detail. Such reactions are uncommon but not without precedent. One of the most well-known simple examples, of biological interest, is the proton-induced disproportionation of the superoxide ion.[63,64] An organic example is the two-proton-induced disproportionation of 4,4′-diiodohydrazobenzene.[65] Phosphododecamolybdate ions disproportionate under the influence of protons.[66] Proton-induced disproportionation reactions of a lutetium bis-phthalocyanine are also known.[67] Some platinum complexes disproportionate in acidic solution.[68,69] As a complementary aside, *base*-induced disproportionation has been observed, for example, with a biological *o*-quinone[70] and with cobalt phthalocyanine.[71,72]

It is worth reassessing biological and catalytic mechanisms involving quinonoid noninnocent ligands with a view to assessing whether such disproportionation may play a role in a pH gradient.

EXPERIMENTAL SECTION

X-ray Data. Crystallographic data were collected at 150 K using a Nonius Kappa CCD diffractometer, with a Mo Kα radiation source (λ = 0.71073 Å). Intensity data were corrected for absorption effects prior to use in calculations. Initial structure solutions were obtained via direct methods, using SHELXL97, while full-matrix least-squares refinement was performed on F^2. All hydrogen atoms were placed at ideal positions, with thermal parameters constrained to ride on their parent atoms, using $U_{iso}(H) = 1.2U_{eq}(C/N)$ for parent sp^2 hybridized carbon or nitrogen atoms, and $1.5U_{eq}(N)$ for parent sp^3 hybridized nitrogen atoms (see Table 1). Crystallographic parameters have been deposited at the Cambridge Crystallographic Data Centre (CCDC).

Direct current (DC) magnetic susceptibility measurements were performed on a Quantum Design SQUID magnetometer (Model MPMS-XL) in Ottawa, Canada, operating between 1.8 K and 400 K for DC applied fields ranging from −7 T to 7 T. Measurements were performed on finely ground polycrystalline samples of 20 mg tightly restrained in a polyethylene membrane. Diamagnetic corrections were applied for the sample holder and the core diamagnetism from the sample (estimated with Pascal's constants).

Raman spectra were measured with a Renishaw Invia Raman imaging microscope (at the Reber Laboratory in Montreal, Canada), using excitation wavelengths of 488 and 782 nm. The microscope was used to focus the light onto a spot ∼1 μm in diameter and to collect the scattered light. The backscattered Raman light was detected with a Peltier cooled CCD detector. Samples were kept at room temperature.

Electron paramagnetic resonance (EPR) spectra were recorded as frozen (77 K) solutions on a Varian Model E4 spectrometer calibrated with diphenylpicrylhydrazyl radical.

UV-vis spectra were recorded with a Hewlett−Packard Model HP8452A diode array, or a Perkin−Elmer Model Lambda 25 spectrometer.

Mass spectra were collected with a ABSciex (Concord, Ontario, Canada) QStar "Elite" QqTOF mass spectrometer operating in positive-ion, MS-only mode. The source voltage was 5 kV, the orifice potential was 30 V, and the ring potential was 90 V. Spectra were obtained at a resolution of ∼12 000, with a mass accuracy of ∼6 ppm.

FT-IR spectra were obtained using KBr disks with a Mattson Genesis II infrared spectrometer.

Cyclic voltammetry were recorded with an Obbligato Objectives Faraday MP potentiostat, or a Pine RDE3 bipotentiostat employing an EDAQ e-corder and software. The working electrode was a platinum wire; a graphite rod was used as the counter electrode, and a pseudo-reference Ag/AgCl electrode was employed. Ferrocene served as an internal reference. The corrections employed were those provided by Geiger.[73]

Spectroelectrochemistry was performed in a 1-cm quartz cell with methanol solvent containing 0.1 M TBAPF6, using a gold or platinum foil as the working electrode, a platinum counter electrode, and an AgCl/Ag wire as the reference electrode. UV-vis spectra were collected therefrom, using an Ocean Optics Model HR2000 high-resolution fiber-optic spectrometer.

Density functional theory (DFT) calculations utilized the Gaussian 09 (Revision B.01 and C.01) program.[74] Optimized geometries were calculated using the B3LYP exchange-correlation functional[75] with the LANL2DZ basis set[76] and the def2-TZVP basis sets.[77] Tight SCF convergence criteria (10^{-8} a.u.) were used for all calculations. Wave functions were checked for stability. Vibrational frequency (FREQ) calculations were also carried out to ensure that the stationary points were truly minima.

Molecular orbital (MO) compositions were calculated using the AOMix program,[44,78] using the Mulliken scheme.[44,79−82] Atomic charges were calculated using the Mulliken[79−82] and natural population analysis[83] methods (MPA and NPA, respectively), as implemented in Gaussian 09, Revisions B.01 and C.01. Extended-charge decomposition analysis was performed using AOMix-CDA.[77,84] The PCM[85,86] was used to model solvation for methanol as a solvent.

Time-dependent DFT (TD-DFT)[55,87−89] was used to calculate the energies and intensities of the 80 lowest-energy electronic transitions of both complexes. These were converted with the SWizard program[90] into simulated spectra, using Gaussian functions with half-widths 2000 cm^{-1}.

Synthesis of [$Ru^{III}(NH_3)_2$(bqdi)Cl_2]Cl (II). Concentrated HCl (5 mL,12 M) was added to (0.0314 g, 0.010 mmol) of $Ru(NH_3)_2$(bqdi)-Cl_2 (**I**).[23] The initial red powder instantly changed to a black mixture. This mixture was stirred in air at room temperature for 24 h. The insoluble product (**II**) (dark green, almost black in color) was separated by centrifuge, washed with diethyl ether, and then vacuum-dried. The yield of green black species **II** as chloride salt was 0.0146 g (83%, based on the disproportionation reaction in eq 1). Concentrated HCl (0.5 mL) was added to the filtrate (4.5 mL) from the preparation of **II**, and the solution was kept at a temperature of ∼3−4 °C for 1 month. This solution produced dark-brown needle-shaped crystals of species **II** (from the remaining **II** in solution) with dimensions of 0.20, 0.10, and 0.06 mm, which were used for the X-ray analysis. Analytical data for $C_6H_{12}Cl_3N_4Ru$: C, 20.7%; H, 3.48%; N, 16.12%. Found: C, 20.35%; H, 3.73%; N, 15.59%. Electrospray mass spectrum parent cation: obs. *m*/*e* 311.9213, calc. *m*/*e* 311.9482. The isotopic pattern of peaks is in accordance with the molecular formula.

Synthesis of [$Ru^{III}(NH_3)_2$(opda)Cl_2]Cl (III). Species **III** exists in the filtrate of the procedure above (deep red solution). It was isolated by freeze-drying of the filtrate. The yield of deep red species **III** as chloride salt was 0.0142 g (81%, based on the disproportionation reaction in eq 1). Electrospray mass spectrum parent cation: obs. *m*/*e* 313.944, calc. *m*/*e* 313.9639. The isotopic pattern of peaks is in accordance with the molecular formula.

Synthesis of [$Ru^{III}(NH_3)_2$(opda)Cl_2]($ZnCl_3(H_2O)$) (IIIc). The filtrate from the preparation of **II** above was mixed with 2 equiv of zinc chloride ($ZnCl_2$). From this solution, purple crystals of a salt that contained the $[ZnCl_3(H_2O)]^-$ anion were obtained. The X-ray data were recorded at 150(1) K with a purple crystal having dimensions of 0.30, 0.20, and 0.07 mm. Attempts to dry these crystals for CHN analysis led to some decomposition.

■ ASSOCIATED CONTENT

Ⓢ Supporting Information

Complete Raman data, and magnetic data for species **II** and detailed TD-DFT calculations and percent contributions to frontier orbitals for both species are included. The $AgNO_3$ oxidation of species **I** to **II** is shown. The complete author list for ref 74 is provided. XYZ coordinates and SCF energies are provided for the DFT optimized species **II** and **III**. The respective numbers for the CIF files deposited with the Cambridge Crystallographic Data Center (CCDC) are CCDC 881048 and CCDC 881047 for [Ru(III)$(NH_3)_2$(bqdi)Cl_2]Cl and [Ru(III)$(NH_3)_2$(opda)Cl_2][$Zn(H_2O)Cl_3$], respectively. This material is available free of charge via the Internet at http://pubs.acs.org.

■ AUTHOR INFORMATION

Corresponding Author

*E-mail: blever@yorku.ca.

Notes

The authors declare no competing financial interest.

■ ACKNOWLEDGMENTS

We thank the Natural Sciences and Engineering Research Council (NSERC, OTTAWA) for financial support. We thank Johnson Matthey for the generous loan of ruthenium trichloride, Dr. Alan Lough (University of Toronto) for acquisition of the X-ray diffraction data, and Dr. Yan Suffren and Prof. Christian Reber (Université de Montreal) for collection of the resonance Raman data. We are also indebted to Dr. Po-Heng Lin, and Prof. Muralee Murugesu (University of Ottawa) for collecting the magnetic data on species **II**. We thank Raluca Popescu for some early experimental data on this system. C.D. thanks the government of Ontario for a postgraduate scholarship. Computing was performed through the courtesy of the Shared Hierarchical Academic Research Computing Network [SHARCNET], Ontario, Canada.

■ REFERENCES

(1) Matz, K. G.; Mtei, R. P.; Rothstein, R.; Kirk, M. L.; Burgmayer, S. J. N. *Inorg. Chem.* **2011**, *50*, 9804.

(2) Basu, P.; Burgmayer, S. J. N. *Coord. Chem. Rev.* **2011**, *255*, 1016−1038.

(3) Burgmayer, S. J. N. *Prog. Inorg. Chem.* **2004**, *52*, 491.

(4) Sun, X.; Chun, H.; Hildenbrand, K.; Bothe, E.; Weyhermüller, T.; Neese, F.; Wieghardt, K. *Inorg. Chem.* **2002**, *41*, 4295−4303.

(5) Shimazakia, Y. *Indian J. Sci.* **2011**, *50A*, 383−394.

(6) Mukherjee, C.; Weyhermüller, T.; Bothe, E.; Chaudhuri, P. *Inorg. Chem.* **2008**, *47*, 11620−11632.

(7) Bugarcic, T.; Habtemariam, A.; Deeth, R. J.; Fabbiani, F. P. A.; Parsons, S.; Sadler, P. J. *Inorg. Chem.* **2009**, *48*, 9444−9453.

(8) Kaim, W.; Schwederski, B. *Coord. Chem. Rev.* **2010**, *254*, 1580−1588.

(9) Tondreau, M.; Milsmann, C.; Lobkovsky, E.; Chirik, P. J. *Inorg. Chem.* **2011**, *50*, 9888.

(10) Heyduk, A. F.; Zarkesh, R. A.; Nguyen, A. I. *Inorg. Chem.* **2011**, *50*, 9849.

(11) Smith, A. L.; Hardcastle, K. I.; Soper, J. D. *J. Am. Chem. Soc.* **2010**, *132*, 14358.

(12) Dzik, W. I.; Xu, X.; Zhang, X. P.; Reek, J. N. H.; de Bruin, B. *J. Am. Chem. Soc.* **2010**, *132*, 10891.

(13) Nguyen, A. I.; Zarkesh, R. A.; Lacy, D. C.; Thorson, M. K.; Heyduk, A. F. *Chem. Sci.* **2011**, *2*, 166.

(14) Sylvester, K. T.; Chirik, P. J. *J. Am. Chem. Soc.* **2009**, *130*, 8772.

(15) Boyer, J. L.; Rochford, J.; Tsai, M.-K.; Muckerman, J. T.; Fujita, E. *Coord. Chem. Rev.* **2010**, *254*, 309−330.

(16) Ringenberg, M. R.; Kokatam, S. L.; Heiden, Z. M.; Rauchfuss, T. B. *J. Am. Chem. Soc.* **2008**, *130*, 788−789.

(17) Adhikari, D.; Mossin, S.; Basuli, F.; Huffman, J. C.; Szilagyi, R. K.; Meyer, K.; Mindiola, D. J. *J. Am. Chem. Soc.* **2008**, *130*, 3676−3682.

(18) Boyer, J. L.; Cundari, T. R.; DeYonker, N. J.; Rauchfuss, T. B.; Wilson, S. R. *Inorg. Chem.* **2009**, *48*, 638−645.

(19) Dzik, W. I.; van der Vlugt, J. I.; Reek, J. N. H.; de Bruin, B. *Angew. Chem., Int. Ed.* **2011**, *50*, 3356−3358.
(20) De Boer, S. Y.; Gloaguen, Y.; Lutz, M.; van der Vlugt, J. I. *Inorg. Chim. Acta* **2012**, *380*, 336−342.
(21) Roy, S.; Blane, T.; Lilio, A.; Kubiak, C. P. *Inorg. Chim. Acta* **2011**, *374*, 134−139.
(22) Arion, V.; Wieghardt, K.; Weyhermüller, T.; Bill, E.; Leovac, V.; Rufinska, A. *Inorg. Chem.* **1997**, *36*, 661−669.
(23) Rusanova, J.; Rusanov, E.; Gorelsky, S. I.; Christendat, D.; Popescu, R.; Farah, A. A.; Beaulac, R.; Reber, C.; Lever, A. B. P. *Inorg. Chem.* **2006**, *45*, 6246−6262.
(24) Mayer, R. G.; Drago, R. S. *Inorg Chem.* **1976**, *15*, 2010.
(25) Boyd, P.; Gerloch, M.; Sheldrick, G. M. *J. Chem. Soc. Dalton Trans.* **1974**, 1097.
(26) Maeda, M.; Ito, T.; Hori, M.; Johansson, G. *Z. Naturforsch., A: Phys. Sci.* **1996**, *51*, 63−70.
(27) Curtis, N. F.; Flood, K.; Robinson, W. T.; Waters, J. M. *Polyhedron* **2009**, *28*, 2103−2112.
(28) Sahami, S.; Weaver, M. J. *J. Solution Chem.* **1981**, *10*, 199−208.
(29) Lever, A. B. P. *Inorg. Chem.* **1990**, *29*, 1271.
(30) Kundu, T.; Sarkar, B.; Mondal, T. K.; Mobin, S. M.; Urbanos, F. A.; Fiedler, J.; Jimenez-Aparicio, R.; Kaim, W.; Lahiri, G. K. *Inorg. Chem.* **2011**, *50*, 4753−4763.
(31) Wada, T.; Yamanaka, M.; Fujihara, T.; Miyazato, Y.; Tanaka, K. *Inorg. Chem.* **2006**, *45*, 8887−8894.
(32) Haga, M.-A.; Isobe, K.; Boone, I. S. R.; Pierpont, C. G. *Inorg. Chem.* **1990**, *29*, 3795−3799.
(33) Auburn, P. R.; Dodsworth, E. S.; Haga, M.; Liu, W.; Nevin, W. A.; Lever, A. B. P. *Inorg. Chem.* **1991**, *30*, 3502−3512.
(34) Ye, S.; Sarkar, B.; Duboc, C.; Fiedler, J.; Kaim, W. *Inorg. Chem.* **2005**, *44*, 2843−2847.
(35) Masui, H.; Lever, A. B. P.; Auburn, P. R. *Inorg. Chem.* **1991**, *30*, 2402−1240.
(36) Lever, A. B. P.; Auburn, P.; Dodsworth, E. S.; Haga, M.; Nevin, W. A. *J. Am. Chem. Soc.* **1988**, *110*, 8076−8084.
(37) Patra, S.; Sarkar, B.; Mobin, S. M.; Kaim, W.; Lahiri, G. K. *Inorg. Chem.* **2003**, *42*, 6469−6473.
(38) Kurihara, M.; Daniele, S.; Tsuge, K.; Sugimoto, H.; Tanaka, K. *Bull. Chem. Soc. Jpn.* **1998**, *71*, 867−875.
(39) Clarke, M. J.; Bailey, N. M.; Doan, P. F.; Hiller, C. D.; LaChance-Galang, K. J.; Daghlian, H.; Mandal, S.; Bastos, C. M.; Lang, D. *Inorg. Chem.* **1996**, 4896−4903.
(40) DeSimone, R. E. *J. Am. Chem. Soc.* **1973**, *95*, 6238−6244.
(41) McKinnon, S. D. J.; Patrick, B. O.; Lever, A. B. P.; Hicks, R. G. *J. Am. Chem. Soc.* **2011**, *133*, 13587−13603.
(42) Gorelsky, S. I.; Lever, A. B. P. *Int. J. Quantum Chem.* **2000**, *80*, 636−645.
(43) Gorelsky, S. I.; Lever, A. B. P.; Ebadi, M. *Coord. Chem. Rev.* **2002**, *230*, 97−105.
(44) Gorelsky, S. I.; Lever, A. B. P. *J. Organomet. Chem.* **2001**, *635*, 187−196.
(45) Li, J.; Xu, L.-C.; Chen, J.-C.; Zheng, K.-C; Ji, L.-N. *J. Phys. Chem. A* **2006**, *110*, 8174−8180.
(46) Remenyi, C.; Kaupp, M. *J. Am. Chem. Soc.* **2005**, *127*, 11399−11413.
(47) Al-Noaimi, M.; El-khateeb, M.; Haddad, S. F; Sunjuk, M.; Crutchley, R. J. *Polyhedron* **2008**, *27*, 3239−3246.
(48) Ess, D. H; Gunnoe, T. B.; Cundari, T. R.; Goddard, W. A., III; Periana, R. A. *Organometallics* **2010**, *29*, 6801−6815.
(49) Futera, Z.; Klenko, J.; Sponer, J. E.; Sponer, J.; Burda, J. V *J. Comput. Chem.* **2009**, *30*, 1758−1770.
(50) Aguilar, C. M.; Rocha, W. R. *J. Phys. Chem. B* **2011**, *115*, 2030−2037.
(51) Chval, Z.; Futera, Z.; Burda, J. V. *J. Chem. Phys.* **2011**, *134*, 024520-1−024520-10.
(52) Weigend, F.; Ahlrichs, R. *Phys. Chem. Chem. Phys.* **2005**, *7*, 3297.
(53) (a) Lever, A. B. P. *Inorganic Electronic Spectroscopy*, 2nd Edition; Elsevier Science: Amsterdam, 1984. (b) Lever, A. B. P.; Walker, I. M.; McCarthy, P. J. *Inorg. Chim. Acta* **1980**, *39*, 81−90.
(54) Wertz, J. E.; Bolton, J. R. *Electron Spin Resonance, Elementary Theory and Practical Applications*; McGraw−Hill: New York, 1972 (ISBN 0070694540).
(55) Casida, M. E.; Huix-Rotllant, M. *Annu. Rev. Phys. Chem.* **2012**, *63*, 287−323.
(56) Ipatov, A.; Cordova, F.; Doriol, L. C.; Casida, M. E. *J. Mol. Struct. THEOCHEM* **2009**, *914*, 60−73.
(57) Beaulac, R.; Lever, A. B. P.; Reber, C. *Eur. J. Inorg. Chem.* **2007**, 48−52.
(58) (a) Brown, G. M.; Weaver, T. R.; Keene, F. R.; Meyer, T. J. *Inorg. Chem.* **1976**, *15*, 190. (b) Keene, F. R. *Coord. Chem. Rev.* **1999**, *187*, 121−149.
(59) Lewars, E. G. *Computational Chemistry*, 2nd Edition; Springer: New York, 2011.
(60) Kalinina, D.; Dares, C.; Kaluarachchi, H.; Potvin, P. G.; Lever, A. B. P. *Inorg. Chem.* **2008**, *47*, 10110−10126.
(61) Earley, J. E.; Fealey, T. *Inorg. Chem.* **1973**, *12*, 323.
(62) Sawyer, D. T.; Roberts, J. L., Jr. *Acc. Chem. Res.* **1988**, *21*, 469−476.
(63) Chin, D. H.; Chiericato, G., Jr.; Nanni, E. J., Jr.; Sawyer, D. T *J. Am. Chem. Soc.* **1982**, *104*, 1296−1299.
(64) Yamaguchi, K. S.; Spencer, L.; Sawyer, D. T. *FEBS Lett.* **1986**, *197*, 249−252.
(65) Shine, H. J.; Habdas, J.; Kwart, H.; Brechbiel, M.; Horgan, A. G.; San, F. J., Jr. *J. Am. Chem. Soc.* **1983**, *105*, 2823−2827.
(66) Artero, V.; Proust, A.; Eur., J. *Inorg. Chem.* **2000**, 2393−2400.
(67) Rimboud, M.; Elleouet, C.; Quentel, F.; Kerbaol, J.-M.; L'Her, M. J. *Electroanal. Chem.* **2008**, *622*, 233−237.
(68) Sakai, K.; Tsubomura, T.; Matsumoto, K. *Inorg. Chim. Acta* **1993**, *213*, 11−16.
(69) Lempers, E. L. M.; Inagaki, K.; Reedijk, J. *Inorg. Chim. Acta* **1988**, *152*, 201−207.
(70) Mandal, S.; Lee, Y.; Purdy, M. M.; Sayre, L. M. *J. Am. Chem. Soc.* **2000**, *122*, 3574−3584.
(71) Liu, W.; Hempstead, M. R.; Nevin, W. A.; Melnik, M.; Lever, A. B. P.; Leznoff, C. C. *J. Chem. Soc., Dalton Trans.* **1987**, 2511−2518.
(72) Nevin, W. A.; Liu, W.; Greenberg, S.; Hempstead, M. R.; Marcuccio, S. M.; Melnik, M.; Leznoff, C. C.; Lever, A. B. P. *Inorg. Chem.* **1987**, *26* (6), 891−899.
(73) Connelly, N. G.; Geiger, W. E. *Chem. Rev.* **1996**, *96*, 877−910.
(74) *Gaussian 09, Revision B.01, C.01*, Frisch, M. J. et al. Gaussian, Inc.: Wallingford, CT, 2009.
(75) Lee, C.; Yang, W.; Parr, R. G. *Phys. Rev. B* **1988**, *37*, 785−789.
(76) (a) Dunning, T. H., Jr.; Hay, P. J. *Modern Theoretical Chemistry*; Schaefer, H. F., III, Ed.; Plenum, New York, 1976, p 1. (b) Hay, P. J.; Wadt, W. R. *J. Chem. Phys.* **1985**, *82*, 270−283. (c) Hay, P. J.; Wadt, W. R. *J. Chem. Phys.* **1985**, *82*, 284−298. (d) Hay, P. J.; Wadt, W. R. *J. Chem. Phys.* **1985**, *82*, 299−310.
(77) *EMSL Basis Set Exchange*, https://bse.pnl.gov/bse/portal.
(78) Gorelsky, S. I. *AOMix-CDA Program*, 2005 (http://www.sg-chem.net/).
(79) Mulliken, R. S. *J. Chem. Phys.* **1955**, *23*, 2338−2342.
(80) Mulliken, R. S. *J. Chem. Phys.* **1955**, *23*, 1833−1840.
(81) Mulliken, R. S. *J. Chem. Phys.* **1955**, *23*, 1841−1846.
(82) Mulliken, R. S. *J. Chem. Phys.* **1955**, *23*, 2343−2346.
(83) (a) Reed, A. E.; Curtiss, L. A.; Weinhold, F. *Chem. Rev.* **1988**, *88*, 899. (b) Glendening, E. D.; Reed, A. E.; Carpenter, J. E.; Weinhold, F. NBO Version 3.1, incorporated within Gaussian 09.
(84) Gorelsky, S. I.; Ghosh, S.; Solomon, E. I. *J. Am. Chem. Soc.* **2006**, *128*, 278.
(85) Noodleman, L.; Lovell, T.; Han, W. G.; Liu, T.; Torres, R. A. *Comprehensive Coordination Chemistry II*; Elsevier: Oxford, U.K., 2004; pp 491−510.
(86) Bickelhaupt, F. M.; Baerends, E. J. *Reviews in Computational Chemistry 15*; Lipkowitz, K. B., Boyd, D. R., Eds.; Wiley: New York, 2000; pp 1−86.
(87) Stratmann, R. E.; Scuseria, G. E.; Frisch, M. J. *J. Chem. Phys.* **1998**, *109*, 8218.
(88) Bauernschmitt, R.; Ahlrichs, R. *Chem. Phys. Lett.* **1996**, *256*, 454.

(89) Casida, M. E.; Jamorski, C.; Casida, K. C.; Salahub, D. R. *J. Chem. Phys.* **1998**, *108*, 4439.

(90) Gorelsky, S. I. *SWizard program*; University of Ottawa: Ottawa, Canada, 2010 (http://www.sg-chem.net/).